

LocalScore: Local Density-Aware Similarity Scoring for Biometrics

Yiyang Su¹ Minchul Kim¹ Jie Zhu¹ Christopher Perry¹
 Feng Liu² Anil Jain¹ Xiaoming Liu^{1,3}

¹ Michigan State University ² Drexel University ³ University of North Carolina, Chapel Hill
 {suyiyan1, kimminc2, zhujie4, perrych2}@msu.edu, f1397@drexel.edu, liuxm@cs.unc.edu

Abstract

Open-set biometrics faces challenges with probe subjects who may not be enrolled in the gallery, as traditional biometric systems struggle to detect these non-mated probes. Despite the growing prevalence of multi-sample galleries in real-world deployments, most existing methods collapse intra-subject variability into a single global representation, leading to suboptimal decision boundaries and poor open-set robustness. To address this issue, we propose LocalScore, a simple yet effective scoring algorithm that explicitly incorporates the local density of the gallery feature distribution using the k -th nearest neighbors. LocalScore is architecture-agnostic, loss-independent, and incurs negligible computational overhead, making it a plug-and-play solution for existing biometric systems. Extensive experiments across multiple modalities demonstrate that LocalScore consistently achieves substantial gains in open-set retrieval (FNIR@FPIR reduced from 53% to 40%) and verification (TAR@FAR improved from 51% to 74%). We further provide theoretical analysis and empirical validation explaining when and why the method achieves the most significant gains based on dataset characteristics.

1. Introduction

Biometrics involves identifying individuals through physical or behavioral characteristics, such as facial features [23], gait patterns [49], and body shape [68]. It is integral to applications ranging from access control to surveillance [46]. At the core, biometric systems compute similarity scores to assess how closely a probe matches enrolled subjects in a gallery. Verification determines whether a probe matches a specific gallery subject and retrieval ranks all gallery subjects by similarity to the probe.

In biometric retrieval, early work focused on closed-set retrieval, where all probe subjects are assumed to exist in the gallery (*i.e.*, mated). In contrast, open-set search represents a more realistic generalization, as the model must accurately identify mated probes while rejecting non-mated

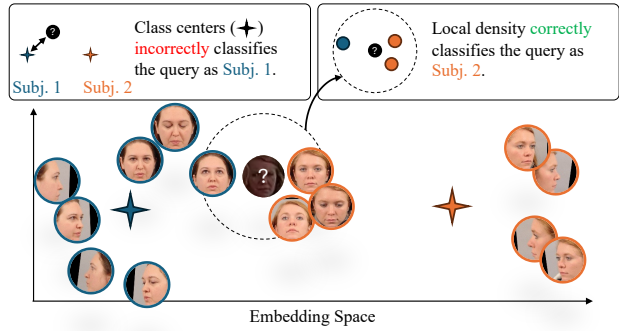


Figure 1. Illustration of the effect of local density in face recognition. Each face represents a gallery feature, and distinct clusters correspond to different viewpoints. Conventional biometric systems only represent each subject by a single class center (shown as the stars). However, a probe sample may lie close to this center yet remain far from all actual clusters, leading to false acceptance in verification or open-set retrieval. In contrast, the local density of the gallery feature distribution captures the true intra-subject variability and correctly rejects such non-mated probes.

ones. These requirements make open-set retrieval inherently more challenging than closed-set retrieval, which only concerns within-gallery identification. Open-set evaluation has been recognized as one of the most challenging scenarios in biometrics [18]. While state-of-the-art (SoTA) whole-body biometric system achieving over 90% closed-set Rank-20 accuracy, when only 1% of non-mated probes are incorrectly identified as mated, it still fails to correctly identify about 55% of mated probes [38]. Hence, in this paper, we focus on open-set retrieval and verification.

In real-world deployments, it is increasingly feasible and common to collect, process, and store multiple samples for each enrolled identity, making the multi-sample gallery setting valid and practically relevant. Therefore, modern large-scale biometric galleries tend to have multiple samples per subject [47]. For example, CCPG [36] includes 33 videos per gallery subject on average.

Despite this, most biometric methods have not explicitly explored how to leverage multi-sample galleries. Existing approaches are often simplistic, relying on score averaging

across gallery samples [44] or assuming that each subject can be represented by a single aggregated feature embedding [28, 52]. These models extract biometric features from input samples (*e.g.*, images or videos) and then aggregate them into a single class center per subject, overlooking the intra-subject variation in multi-sample galleries.

Naïvely averaging gallery feature embeddings or scores fails to capture that subject’s true variability. As illustrated in Fig. 1 (top-left), such approaches rely solely on similarity to a subject’s global center, ignoring the diverse conditions (*e.g.*, pose, illumination, viewpoint) that produce distinct clusters within the same subject. Consequently, collapsing multi-cluster gallery distributions into a single center leads to suboptimal decision boundaries and degraded discrimination. This limitation is particularly detrimental in open-set scenarios, where accurately rejecting unseen subjects requires modeling the full extent of intra-subject variation.

To illustrate this issue, Fig. 1 presents a face recognition example in which exemplar subjects’ gallery embeddings form several distinct clusters associated with different camera viewpoints. A probe may lie near the center of subject #1 yet remain relatively far from its clusters, leading to a false acceptance of a non-mated sample. Conversely, a genuine probe from an underrepresented cluster may be erroneously rejected. These failure cases highlight the limitations of relying solely on class centers and motivate the need for methods that leverage the *local density* of gallery features to more accurately reflect intra-subject variation.

We propose LocalScore, a novel scoring framework that models intra-subject variability through local structure rather than global averaging in biometric systems. The key idea is that the k -th nearest neighbor (k -NN) provides a simple yet effective way to capture the local geometry of a subject’s gallery features. As shown in Fig. 1, a non-mated probe may lie near the global gallery center yet remain distant from all true clusters, causing traditional center-based scoring to falsely accept it. LocalScore addresses this by assessing how well a probe aligns with the local neighborhoods of genuine gallery samples using k -NN. Probes distant from their nearest neighbors are more likely imposters, while genuine probes tend to be closer. By leveraging the local gallery structure, LocalScore substantially improves verification accuracy and open-set robustness. Moreover, LocalScore is easily deployable, implemented in just a single line of code. It is a plug-and-play module compatible with any biometric model, independent of architecture or loss function, and introduces negligible computational overhead.

We evaluate LocalScore across three major biometric modalities—face recognition, gait recognition, and person reID using diverse model architectures, including ResNet [16], ViT [39, 64], and Swin Transformer [11]. These models are trained with various loss functions such as cross-entropy variants [27] and triplet loss [20]. Across all

settings, LocalScore consistently surpasses standard scoring methods, delivering substantial gains in both open-set performance (reducing FNIR@FPIR from 53% to 40%) and verification accuracy (raising TAR@FAR from 51% to 74%).

Additionally, we present comprehensive theoretical and empirical analyses to investigate the behavior of our proposed algorithm. Theoretically, we model the expected performance with and without LocalScore based on score statistics and provide guidance on the conditions under which LocalScore is expected to enhance open-set biometrics and verification. Empirically, we validate the soundness of our theoretical insights on real-world datasets and through Monte Carlo simulations and examine the impact of k in k -NN and intra-subject variations on performance. We find that the algorithm consistently improves performance across a wide range of conditions and underscores its robustness.

We summarize our contributions as follows:

- We propose LocalScore, that incorporates the local gallery density information on gallery feature distribution around each probe into biometric scores.
- We validate the superior performance of our method across a variety of biometric models and tasks, significantly enhancing recognition accuracy.
- We present detailed analyses comparing traditional distance metrics and our algorithm in theory, through simulations on synthetic datasets, and on real-world datasets.

2. Related Work

Biometrics. Biometric recognition has been extensively studied across modalities such as face recognition [9, 30, 32, 43, 66], gait recognition [19, 21, 24, 50, 59, 63, 65], person reID [5, 8, 26, 35, 37, 42, 53, 57, 60, 67, 69], and combination of modalities [31, 38, 40, 73]. Most prior work focuses on designing network architectures or loss functions to obtain more discriminative representations. However, scoring typically relies on the subjects’ aggregated gallery centers, overlooking the underlying structure of the gallery features. In contrast, we introduce LocalScore, which leverages the local density of gallery features to produce more reliable similarity scores. Also, while many existing methods emphasize verification or closed-set retrieval, only a few [17, 52] explicitly address the more challenging open-set setting.

Open-Set Recognition. Open-set recognition [3, 7, 33, 34, 45, 56, 58] aims to distinguish between known and unknown classes in image classification. As noted in [52], the known classes correspond to those in the training set, while the unknown classes are those not used for training [13]. In contrast, even in closed-set biometrics, the test subjects are not used for training, and mated probes are test subjects enrolled in the gallery [22]. Open-set biometrics differs from closed-set biometrics in that non-mated subjects do not appear in either the training set or the gallery [15, 17].

While previous studies have explored the use of k -NN for out-of-distribution (OOD) detection [54] and open-set recognition [61], k -NN scores alone do not have sufficient discriminative information for biometric recognition. In contrast, our approach leverages k -NN to model the local feature density around probes and integrates this density measure into biometric scoring.

Re-ranking. Re-ranking [1, 2, 41, 48, 51, 55, 62, 70, 72] enhances the original ranking of probes obtained from a pretrained person reID model. Notably, [72] improves performance by considering if the probe is among the closest neighbors of the galleries. Although re-ranking can be applied to various biometric modalities, it depends on a large set of probes or queries to function effectively. However, in real-world applications, probes are often received continuously, and their distribution is unknown. As a result, the theoretical foundation and performance of re-ranking suffer when only one probe is available. In contrast, our method processes each probe independently, without requiring other probes. Further, our method is more computationally efficient than re-ranking due to its simplicity.

3. Method

3.1. Problem Setup

Consider a gallery with N subjects, each with multiple samples (*e.g.*, images or videos). For the i -th subject, the biometric features are $\mathbf{g}_i^1, \dots, \mathbf{g}_i^{m_i} \in \mathbb{R}^d$, and the full gallery is $\mathcal{G} = \{\mathbf{g}_i^j \mid 1 \leq i \leq N, 1 \leq j \leq m_i\}$. Given a query $\mathbf{q} \in \mathbb{R}^d$, the goal is to compute $\mathbf{s} = f(\mathbf{q}, \mathcal{G})$, where each \mathbf{s}_i measures similarity between \mathbf{q} and subject i . The design of f directly influences verification and open-set retrieval performance.

A common strategy [52] represents each subject with a single aggregated feature:

$$\mathbf{s}_i = \left\langle \frac{\mathbf{q}}{\|\mathbf{q}\|}, \frac{1}{m_i} \sum_{j=1}^{m_i} \frac{\mathbf{g}_i^j}{\|\mathbf{g}_i^j\|} \right\rangle. \quad (1)$$

Methods such as EVM [17] and CAFace [28] follow this principle, differing only in aggregation details. However, all collapse intra-subject variation into a single prototype, discarding the feature distribution's structure.

Alternatively, one can average per-sample similarities:

$$\mathbf{s}'_i = \frac{1}{m_i} \sum_{j=1}^{m_i} \left\langle \frac{\mathbf{q}}{\|\mathbf{q}\|}, \frac{\mathbf{g}_i^j}{\|\mathbf{g}_i^j\|} \right\rangle, \quad (2)$$

which retains all samples but treats them equally, ignoring cross-sample correlations or local substructure.

Existing scoring functions compute f independently for each subject, ignoring the gallery distribution. Specifically, conventional similarities assume that a subject's features form a single cohesive cluster, whereas real-world data often

```

def local_score(model, x, G_S, G_M, k):
    """
    Parameters:
    - model: Pretrained biometric model
    - x: Probe input
    - G_S: (N, D) Per-subject gallery database
    - G_M: (N_m, D) Per-media gallery database
    - k: The "k" in KNN

    Returns:
    - (D,) updated score vector
    """

    # (N_g, ) ; similarity scores with G_S
    sim_scores = sim(model(x), G_S)

    # (1,); the k-th nearest neighbor in G_M
    knn_score = sim(model(x), G_M).sort()[:, -k]

    # (N_g, ); output similarity scores
    sim_scores += knn_score * (sim_scores == sim_scores.max())

    return sim_scores

```

Algorithm 1. Python-style pseudo-code for LocalScore.

contain multiple distinct regions corresponding to different viewpoints, illuminations, or other conditions. As a result, probes near sparse areas may appear close to the global mean but misaligned with any true region, leading to false acceptances or rejections. Neglecting this local structure limits the reliability of traditional scoring functions.

3.2. LocalScore

Since gallery features naturally reflect intra-subject variation, we incorporate all samples in \mathcal{G} during scoring to capture the feature patterns within each subject. Instead of averaging gallery features or pairwise similarities across all m_i samples, we focus on the local geometry of each subject's feature space. We find the k -th nearest neighbor of the probe q among the gallery samples and calculate

$$s^{(k)} = \text{top-}k_{i,j} \left(\left\langle \frac{\mathbf{q}}{\|\mathbf{q}\|}, \frac{\mathbf{g}_i^j}{\|\mathbf{g}_i^j\|} \right\rangle \right), \quad (3)$$

where $\text{top-}k(\cdot)$ returns the k -th largest similarity and \mathbf{g}_i^j denotes the j -th feature of subject i . This measures how closely the probe aligns with the most relevant local region of the gallery distribution. Genuine probes tend to yield larger $s^{(k)}$ as they cluster within dense regions of the correct subject's gallery, while imposters tend to lie outside these modes and thus score lower.

To incorporate local geometry while preserving identity information, we fuse the k -NN score with the standard per-subject score \mathbf{s} . A naïve averaging between \mathbf{s}_i and $\mathbf{s}^{(k)}$ degrades performance because $\mathbf{s}^{(k)}$ lacks explicit identity su-

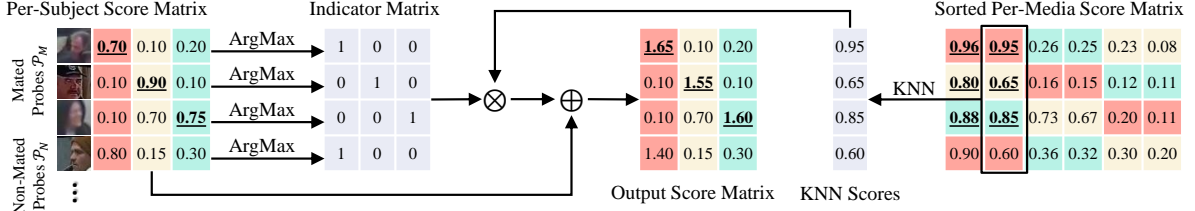


Figure 2. A toy example of LocalScore, where genuine scores are bolded and underscored. Different colors represent different gallery subjects. The k -NN scores are calculated from the per-media score matrix for each probe and added to the maximum per-subject score to generate the output score matrix. For instance, for the first probe, a k -NN score of 0.95 is added to the highest per-subject score of 0.7, while all other scores remain unchanged. In the original score matrix, only one genuine score exceeds the maximum-per-probe non-mated score of 0.8. However, after applying LocalScore, all genuine scores surpass the updated maximum-per-probe non-mated score of 1.4.

pervision, inflating non-match scores and narrowing the genuine-impostor margin. For instance, we find that this naïve fusion strategy reduces TAR@0.1%FAR of KPRPE [29] on the BRIAR dataset [6] from 60% to 30%. Instead, we selectively apply the k -NN adjustment only to the top-scoring subject for each probe.

For instance, as illustrated by the third mated probe in Fig. 2, the similarity to the first subject after naïve mean fusion is $(0.70 + 0.85)/2 = 0.775$. This value equals the similarity between the second probe and its true match (the second gallery subject), $(0.90 + 0.65)/2 = 0.775$. In this example, the first score is a non-match score, while the second is a match score. Thus, the verification performance suffers because the gap between match and non-match scores vanishes, causing fewer probes to be counted as true positives. Therefore, a more sophisticated algorithm is necessary.

To resolve this issue, let $\mathbf{i} \in \{0, 1\}^N$ be an indicator vector where $\mathbf{i}_i = 1$ if $\mathbf{s}_i = \max_j \mathbf{s}_j$ and 0 otherwise. The final fused scores $\mathbf{t} \in \mathbb{R}^N$ are computed as:

$$\mathbf{t} = \mathbf{s} + \mathbf{i} \cdot \mathbf{s}^{(k)}. \quad (4)$$

This selective fusion increases the similarity only for the most probable subject, thereby avoiding global score inflation. LocalScore is presented in Alg. 1. Note that it only capitalizes on the local gallery feature distribution and does not use the label of the gallery samples.

Compared to the naïve fusion strategy, LocalScore increases the similarity scores of only the highest-scoring subject for each probe to avoid the broad inflation of non-match scores. In the toy example shown in Fig. 2, this selective increment keeps the similarity between the third probe and the second gallery subject at 0.70, which is considerably lower than any true match score. As a result, the non-match score does not overlap with the genuine matches. By not inflating the scores of non-top-ranked subjects, LocalScore preserves a wider separation between impostor and genuine distributions, improving verification performance.

LocalScore is training-free, efficient, and fully compatible with existing biometric models. Instead of assuming that a subject’s gallery features form a single cohesive cluster, it

models their local structure, enabling improved verification and open-set recognition without any changes to network architecture or training objectives.

3.3. Gallery Clustering

While incorporating all gallery samples enhances robustness by capturing diverse intra-subject variations, it also increases memory and computation for subjects with many samples. To mitigate this, we optionally cluster each subject’s gallery features into a compact set of representative prototypes, preserving local structure while reducing cost.

For the i -th subject with gallery features $\{\mathbf{g}_i^1, \dots, \mathbf{g}_i^{m_i}\}$, we cluster them into $C_i \ll m_i$ centers $\{\mathbf{c}_i^1, \dots, \mathbf{c}_i^{C_i}\}$, where each center is

$$\mathbf{c}_i^k = \frac{1}{|\mathcal{C}_i^k|} \sum_{\mathbf{g}_i^j \in \mathcal{C}_i^k} \mathbf{g}_i^j, \quad (5)$$

and \mathcal{C}_i^k is the set of features in the k -th cluster. The resulting compact gallery is $\tilde{\mathcal{G}} = \{\mathbf{c}_i^k\}_{i,k}$.

During inference, all similarity computations, including k -NN search and fusion, operate on cluster centers. The per-subject k -NN score becomes

$$\mathbf{s}_i^{(k)} = \text{top-}k_j \left(\left\langle \frac{\mathbf{q}}{\|\mathbf{q}\|}, \frac{\mathbf{c}_i^j}{\|\mathbf{c}_i^j\|} \right\rangle \right), \quad (6)$$

where each \mathbf{c}_i^j captures a local mode of subject i ’s distribution. This compact representation replaces redundant samples with informative prototypes, achieving a favorable balance between accuracy and efficiency.

3.4. Theoretical Analyses

We establish a theoretical framework to define the boundaries of applicability for LocalScore to provide bounds for scenarios where it enhances verification and open-set search. Specifically, Thm. 1 offers a criterion to assess whether the k -NN scores provide sufficient separation between mated and non-mated scores, resulting in improvements in both FNIR@FPIR and TAR@FAR.

Suppose the per-subject genuine scores are normally distributed as $\mathcal{N}(\mu_1, \sigma_1)$. The per-subject imposter scores are distributed as $\mathcal{N}(\mu_2, \sigma_2)$. The k -NN scores for mated probes are distributed as $\mathcal{N}(\mu_3, \sigma_3)$, and the k -NN scores for non-mated probes are distributed as $\mathcal{N}(\mu_4, \sigma_4)$. Also, let N_1 be the number of mated probes, N_2 be the number of non-mated probes, M be the number of gallery subjects, N_3 be the total number of imposter scores, and r_1 and r_2 be the tolerable number of maximum-per-probe non-mated scores (e.g., $1\% \times N_2$) and non-match scores (e.g., $0.1\% \times N_3$).

Theorem 1. *Alg. 1* improves the expected open-set FNIR@FPIR at the expected threshold if

$$\frac{\mu_2 + \mu_4 + \delta \sqrt{\sigma_2^2 + \sigma_4^2} - (\mu_1 + \mu_3)}{\sqrt{\sigma_1^2 + \sigma_3^2}} < \frac{(\mu_2 + \delta \sigma_2) - \mu_1}{\sigma_1}, \quad (7)$$

where $\delta = -\ln(-\ln(1 - r_1/N_2))$ and improves verification TAR@FAR at the expected threshold if

$$\frac{\mu_2 + \mu_4 + \Phi^{-1}\left(\frac{N_3 - r_2 - \alpha}{N_3 - 2\alpha + 1}\right) \sqrt{\sigma_2^2 + \sigma_4^2} - (\mu_1 + \mu_3)}{\sqrt{\sigma_1^2 + \sigma_3^2}} < \frac{\mu_2 + \Phi^{-1}\left(\frac{N_3 - r_2 - \alpha}{N_3 - 2\alpha + 1}\right) \sigma_2 - \mu_1}{\sigma_1}, \quad (8)$$

where $\Phi^{-1}(\cdot)$ is the inverse of the cumulative distribution function of normal distribution, and $\alpha = \pi/8$ is a constant.

For a proof of Thm. 1, please refer to the supplementary.

4. Experiments

Evaluation Protocols. We follow the evaluation protocols (train vs. test, gallery vs. probe, and mated vs. non-mated splits) of [52] whenever possible. For newer datasets, we randomly generate evaluation protocols in the same way.

Evaluation Metrics. We evaluate biometric models from two aspects: verification and open-set retrieval. For verification, we report TAR@FAR at both 0.1% and 1% thresholds. For open-set search, we present the FNIR@FPIR at 0.1% and 1% thresholds for larger datasets and 1% and 5% for smaller ones. Given the inherent variability in FNIR@FPIR [52], we provide their means and 95% confidence intervals from the results of 50 runs.

Datasets. In addition to IJB-S, Gait3D, and CCVID [52], we evaluate on CCPG [36] for RGB-based gait recognition and BRIAR [6] for multi-modal fusion. CCPG targets clothing-changing gait recognition and person reID. It contains 100 training and 100 test subjects with 8,388 and 8,178 sequences, respectively. CCPG provides RGB images with faces and shoes grayed out, enabling RGB-based gait

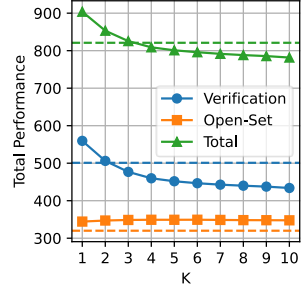


Figure 3. The effect of k on the overall performance. The total performance is the sum of TPIR@FPIR (i.e., 1-FNIR@FPIR), TAR@FAR, and rank-1 accuracy. Dashed lines: without LocalScore.

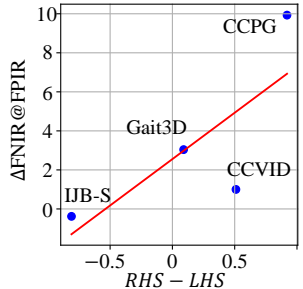


Figure 4. The relationship between performance gains from LocalScore on various datasets and the theoretical difference between the right-hand and the left-hand side of Eq. (7). Red line: linear regression.

recognition methods like BigGait [64], which outperform silhouette-based approaches. BRIAR focuses on long-range and UAV-based biometrics across modalities including face, gait, and person reID. Its training set has 995 subjects, and we follow official protocol v6.1.0 with 1,280 gallery subjects and 6,813 probe sequences to evaluate LocalScore’s performance in whole-body human recognition.

4.1. Ablation Studies

Effect of k . We analyze the sensitivity of verification and open-set recognition performance to k across three modalities: face recognition on BRIAR [6] with IJB-S [25], gait recognition on Gait3D [71] with SwinGait [11], and person reID on CCVID with CAL [16]. Fig. 3 illustrates the summed verification and open-set search performance. The open-set performance remains robust across different k values, indicating that LocalScore generalizes well. For verification, the performance degrades as k increases. In general, smaller k values yield better performance, particularly for datasets with smaller gallery sizes (e.g., Gait3D with only 5.4 sequences per subject on average). Larger values of k tend to degrade verification performance due to an increased chance of including neighbors of incorrect gallery identities for genuine probes. Thus, we choose $k=1$ in our experiments.

Effects of Gallery Clustering. To examine the trade-off between storage and performance, we evaluate clustering of each subject’s gallery prior to scoring. Specifically, the gallery is clustered into C_i clusters using k -means, and each cluster is represented by its centroid.

As shown in Tab. 1, open-set FNIR@FPIR improves as C_i increases. This indicates that broader coverage of a subject’s intra-subject variation reduces false rejections in open-set scenarios. In contrast, verification (TAR@FAR) remains stable across cluster sizes, suggesting that only a few centroids suffice for genuine match identification.

Model	Dataset	C_i	% Gal.	Run-time	FNIR@FPIR ↓		TAR@FAR ↑	
					0.1%	1%	0.1%	1%
SwinGait [11]	Gait3D [†] [36]	N/A	< 1	124	81.84	66.09	57.81	78.95
		5	53.7	246	83.50	69.10	63.65	78.95
		20	92.3	319	81.01	65.43	63.65	79.08
BigGait [64]	CCPG [36]	∞	100	338	78.80	62.98	63.65	79.08
		N/A	< 1	29	46.95	34.53	82.46	95.64
		5	14.2	60	41.04	29.52	92.25	97.00
		20	56.8	175	39.23	27.34	92.89	97.00
		∞	100	301	37.04	25.34	92.95	97.01

Table 1. Open-set FNIR@FPIR and verification TAR@FAR under different C_i . % Gal.: the ratio of the size of the clustered gallery to that of the full gallery. Runtime is reported in milliseconds (ms).

[†]FNIR@FPIR reported at 1% and 5% thresholds.

Sensitivity to clustering varies by dataset. Gait3D [71] has few, highly variable samples per subject (avg. ≈ 5), so clustering offers limited gains. In contrast, CCPG [36], with more samples per subject (avg. ≈ 35) under controlled conditions, achieves near-full performance using under 50% of samples. Thus, redundant gallery features can be compressed with minimal accuracy loss.

In subsequent experiments, we use the full gallery to report the best performance.

4.2. Results

Comparison with SoTA. We evaluate LocalScore using SoTA models across diverse biometric modalities, datasets, and gallery aggregation methods, including CAFace [28] for face and EVM [17], which fits Weibull distributions to gallery features. As shown in Tab. 2, LocalScore consistently improves over the original scores across all settings. On CCPG, for instance, it enhances BigGait from 82.46% to 92.95% (by 10.49%) on TAR@0.1%FAR and from 46.95% to 37.04 (by 9.93%) on FNIR@0.1%FPIR, without degrading performance for any model. When combined with EVM, LocalScore further boosts verification accuracy, *e.g.*, improving TAR@0.1%FAR on Gait3D from 69.68% to 79.84% (by 10.16%), while maintaining low inference cost and requiring only a single hyperparameter.

Theoretical Predictions. Thm. 1 provides a theoretical tool to predict the real-world performance of LocalScore. To validate the accuracy of the theoretical predictions, we compare performance gains from LocalScore to the difference between the right-hand side (RHS) and the left-hand side (LHS) of Eq. (7) in Fig. 4, averaged over multiple gallery sets. The strong correlation (Pearson coefficient 0.77) and large positive slope (4.75) confirm that increases in this theoretical difference align with real-world performance improvements, demonstrating Thm. 1’s predictive power despite its assumptions on score distributions.

1:1 Evaluation. Although standard deployments assume access to all enrolled subjects, certain practical scenarios

restrict verification to a single available subject. To assess whether LocalScore remains effective under this constraint, we evaluate it in a 1:1 setting, where each decision involves a single probe and a single gallery subject. In this setup, our method enhances similarity scores using only the gallery samples of the active subject (see supplementary materials for an illustration). Results for this configuration are reported as Ours* in Tab. 2. Across modalities and datasets, LocalScore delivers strong verification and open-set performance even without access to the full gallery. Surprisingly, its open-set results often surpass those obtained when all subjects are available. For example, on CCPG [36] using BigGait [64], LocalScore achieves 36.29% FNIR@0.1%FPIR, compared to 46.95% without our method and 37.04% when using the entire gallery. For verification, while performance is generally lower than in the full-gallery setting, LocalScore still provides substantial gains over baseline scoring. Notably, on Gait3D [71] with SwinGait [11], it improves TAR@0.1%FAR from 57.81% to 65.62%, whereas using the entire gallery yields only 63.65%. These results demonstrate that LocalScore effectively models intra-subject variation and enables reliable verification even when only a single subject’s gallery is available.

Human Recognition. We evaluate LocalScore across four modalities in the multi-modal BRIAR benchmark: face, gait, person re-identification (reID), and whole-body recognition. Each modality uses its own feature extractor, and results are summarized in Tab. 3. LocalScore yields consistent gains in open-set performance, with especially strong improvements on CCVID. For instance, it reduces FNIR@1%FPIR for reID from 52.77 to 40.49 and boosts TAR@0.1%FAR for gait from 50.72% to 73.98%. On the more challenging BRIAR [6] dataset, LocalScore also improves performance in nearly all cases. These results demonstrate that LocalScore integrates seamlessly into real-world systems, enhancing not only individual models but also complex multi-modal human recognition pipelines.

Comparison with Multi-Sample Methods. We compare our scoring function against standard multi-sample aggregation strategies that collapse multiple gallery samples into a single score. Specifically, we evaluate three methods, mean, max, and min [4]. As shown in Tab. 4, these approaches exhibit a consistent ordering: our method delivers the strongest performance, followed by max, with mean and min trailing behind. For instance, on CCPG [36], our approach achieves the lowest FNIR (37.04%@0.1%FPIR), compared to 42.87% for max, 51.08% for mean, and 83.23% for min. A similar pattern appears in verification performance, where our TAR@0.1%FAR reaches 92.95%, surpassing max (86.94%), mean (79.22%), and min (48.65%). Overall, incorporating local geometric information into the scoring function yields more reliable verification under both

Modality	Model	Dataset	Gallery	Scoring	FNIR@FPIR ↓		TAR@FAR ↑	
					1%	5%	0.1%	1%
Face	KPRPE [29]	IJB-S [25]	Avg	N/A	94.11	88.64	10.69	25.47
				Ours*	94.17	88.00	11.33	25.91
				Ours	94.49	89.12	21.76	45.47
	SwinGait [11]	Gait3D [71]	EVM [17]	N/A	88.20	83.43	18.93	31.83
				Ours*	94.35	83.94	17.76	31.28
				Ours	94.08	84.63	22.93	36.83
Gait	BigGait [64]	CCPG [†] [36]	Avg	N/A	81.84±1.76	66.09±0.69	57.81	78.95
				Ours*	78.59±2.04	61.76±0.94	65.62	86.47
				Ours	78.80±1.99	62.98±0.78	63.65	79.08
	BigGait [64]	CCPG [†] [36]	EVM [17]	N/A	83.63±1.54	62.40±1.26	69.68	88.61
				Ours*	83.36±1.55	61.95±1.23	69.89	92.20
				Ours	83.38±1.53	62.19±1.21	79.84	88.72
ReID	CAL [16]	CCVID [16]	Avg	N/A	46.95±2.02	34.53±1.96	82.46	95.64
				Ours*	36.39±2.77	24.10±2.12	87.86	97.04
				Ours	37.04±2.71	25.34±1.99	92.95	97.01
	BigGait [64]	CCPG [†] [36]	EVM [17]	N/A	46.64±3.93	34.94±3.41	86.25	97.37
				Ours*	41.93±4.14	30.23±3.23	87.13	97.10
				Ours	41.99±4.13	30.41±3.21	93.29	97.78

Table 2. Open-set FNIR@FPIR and verification TAR@FAR on real-world biometric datasets. 95% confidence intervals are reported for FNIR@FPIR. Ours* denotes LocalScore under the 1:1 setting. [†]FNIR@FPIR reported at 0.1% and 1% thresholds.

Task	Model	Ours	FNIR@FPIR ↓		TAR@FAR ↑	
			CCVID	BRIAR	CCVID	BRIAR
Face	KPRPE [29]	✗	12.99	93.6	91.12	14.7
		✓	10.67	92.9	93.88	17.3
Gait	BigGait [64]	✗	71.05	84.3	50.72	35.3
		✓	59.92	84.0	73.98	37.7
ReID	CLIP3D- ReID [39]	✗	52.77	86.8	62.11	28.2
		✓	40.49	87.2	80.46	32.2
Whole Body	FarSight [38]	✗	15.41	76.3	87.41	39.2
		✓	10.74	73.4	91.73	53.5

Table 3. Open-set FNIR@FPIR, verification TAR@FAR on the BRIAR [6] and CCVID [16] datasets.

open- and closed-set conditions than pooling-based methods that ignore intra-subject variation.

Comparison with Re-Ranking. For fair comparison, we evaluate LocalScore against a per-probe variant of the re-ranking algorithm [72], adapted to operate on each probe independently. Classical re-ranking leverages reciprocal neighbors—*i.e.*, mutual nearest-neighbor relationships within a set of queries—and thus typically requires multiple probes to be effective. As shown in Tab. 4, LocalScore consistently surpasses per-probe re-ranking by a substantial margin, un-

Task	Model	Dataset	Method	FNIR@FPIR ↓		TAR@FAR ↑	
				0.1%	1%	0.1%	1%
Gait	BigGait [64]	CCPG [†] [36]	Max	42.87	28.92	86.94	97.11
			Min	83.23	70.97	48.65	77.88
			Mean	51.08	38.12	79.22	95.20
			R-R	47.84	36.56	81.12	95.14
			Ours	37.04	25.34	92.95	97.01
ReID	CAL [16]	CCVID [†] [16]	Max	40.55	32.89	69.65	82.83
			Min	54.49	45.86	60.97	80.36
			Mean	38.74	34.38	69.16	82.87
			R-R	40.52	34.12	68.88	83.60
			Ours	38.98	34.19	75.23	85.34

Table 4. Open-set FNIR@FPIR and verification TAR@FAR of multi-sample methods. [†]FNIR@FPIR reported at 1% and 5% thresholds. [R-R: Re-ranking [72]]

derscoring its suitability for real-world biometric scenarios where probes often arrive individually.

5. Monte Carlo Simulations

5.1. Analysis on Thm. 1

We perform Monte Carlo simulations to assess the practical validity of Thm. 1 under both its theoretical assumptions and more general conditions. Specifically, we generate random

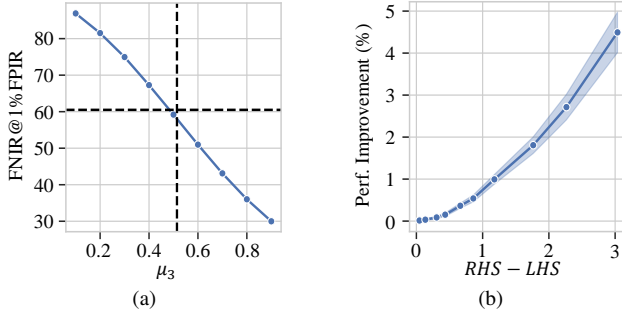


Figure 5. (a) The effect of μ_3 on open-set FNIR@1%FPIR. The vertical line indicates the theoretically predicted μ_3^* , and the horizontal line indicates the performance without our method. (b) The impact of the difference between the RHS and LHS of Eq. (7) on the improvement of FNIR@FPIR by using our method. The shaded area is the 99% confidence interval.

score matrices consistent with Thm. 1’s assumptions, where match, non-match, mated KNN, and non-mated scores follow normal distributions. We then compute μ_3^* , the value that equates the two sides of Eq. (7). Keeping all other distribution parameters fixed, we vary μ_3 and observe in Fig. 5a that performance decreases when $\mu_3 < \mu_3^*$ and improves when $\mu_3 > \mu_3^*$. This alignment between simulation and theory confirms Thm. 1’s predictive validity for identifying when our method yields performance gains.

To account for deviations from our theoretical assumptions, we extend the simulations to randomly generated feature vectors and corresponding score matrices. We examine how performance gains relate to the numerical gap between the RHS and LHS of Eq. (7), where a larger gap indicates greater separation between mated and non-mated k-NN scores, and thus stronger performance improvements.

We create synthetic datasets containing both mated and non-mated samples to evaluate our method. Specifically, 20% of the N classes are designated as non-mated, containing only probe samples. For the i -th class, data are drawn from a multivariate Gaussian:

$$\mathcal{N}\left(\left[\cos\left(\frac{2\pi i}{N}\right), \sin\left(\frac{2\pi i}{N}\right)\right]^T, \sigma^2 \mathbf{I}\right), \quad (9)$$

yielding classes evenly distributed on the unit circle. Mated classes include M samples for both gallery and probe sets, while non-mated classes contain M probe samples only. Here, σ controls intra-class variation and N denotes the total number of classes. Each experiment is repeated 1,000 times with different random seeds for robustness.

Fig. 5b demonstrates that LocalScore reliably separate mated from non-mated probes across varying σ and k . The RHS consistently exceeds the LHS, which is consistent with observed open-set performance gains in most cases. Moreover, larger numerical differences correspond to greater improvements, indicating that despite its normality assumption,

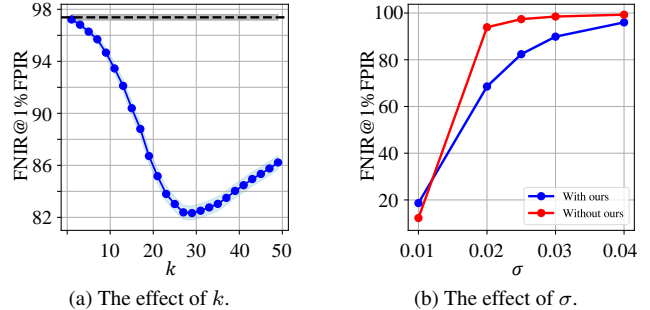


Figure 6. The effect of k and σ on open-set FNIR@1%FPIR. In (a), the horizontal line denotes performance without our method. The shaded area is the 99% confidence interval.

Thm. 1 generalizes well and effectively predicts when our method enhances FNIR@FPIR.

5.2. Ablation Study

We ablate the hyperparameter k and the intra-class variation parameter σ using the same setup as in the previous subsection, reporting their effects on FNIR@1%FPIR. Additional analyses on Eq. (8) and TAR@FAR are provided in the supplementary materials.

Effect of k . As shown in Fig. 6a, open-set FNIR@1%FPIR decreases sharply for small k and then rises gradually. This trend aligns with real-world observations, where LocalScore consistently outperforms the baseline. Compared to our simulations, the optimal k in practice is smaller— $k = 1$ in our experiments. While the Gaussian assumption in simulation may not fully capture real-world feature distributions, our method consistently improves open-set performance, achieving over 15% gains at the optimal k .

Effect of σ . As shown in Fig. 6b, performance gains depend strongly on intra-class variation. For small σ (low variation), improvements are small, but as σ increases, LocalScore rapidly surpasses raw scores, with substantial gains in challenging cases. This pattern aligns with real datasets, where greater benefits occur in modalities with higher intra-subject variation such as gait and person reID. In face recognition, which exhibits lower variation, LocalScore still delivers notable improvements, particularly for verification.

6. Conclusion

We present a simple yet effective algorithm to enhance open-set search and verification performance by leveraging intra-subject variation. We evaluate our method across various biometric tasks, utilizing models with different architectures and trained with diverse loss functions to demonstrate its efficacy. Further, we provide both empirical and theoretical analyses to understand the condition under which our method improves the performance.

Acknowledgements. This research is based upon work supported in part by the Office of the Director of National Intelligence (ODNI), Intelligence Advanced Research Projects Activity (IARPA), via 2022-21102100004. The views and conclusions contained herein are those of the authors and should not be interpreted as necessarily representing the official policies, either expressed or implied, of ODNI, IARPA, or the U.S. Government. The U.S. Government is authorized to reproduce and distribute reprints for governmental purposes notwithstanding any copyright annotation therein.

References

- [1] Song Bai, Peng Tang, Philip H.S. Torr, and Longin Jan Latecki. Re-ranking via metric fusion for object retrieval and person re-identification. In *CVPR*, 2019. 3
- [2] Arko Barman and Shishir K Shah. Shape: A novel graph theoretic algorithm for making consensus-based decisions in person re-identification systems. In *ICCV*, 2017. 3
- [3] Abhijit Bendale and Terrance E Boult. Towards open set deep networks. In *CVPR*, 2016. 2
- [4] Lacey Best-Rowden, Hu Han, Charles Otto, Brendan F Klare, and Anil K Jain. Unconstrained face recognition: Identifying a person of interest from a media collection. *IEEE Transactions on Information Forensics and Security*, 2014. 6
- [5] Keqi Chen, Vinkle Srivastav, Didier Mutter, and Nicolas Padoy. Learning from synchronization: Self-supervised uncalibrated multi-view person association in challenging scenes. In *CVPR*, 2025. 2
- [6] David Cornett, Joel Brogan, Nell Barber, Deniz Aykac, Seth Baird, Nicholas Burchfield, Carl Dukes, Andrew Duncan, Regina Ferrell, Jim Goddard, et al. Expanding accurate person recognition to new altitudes and ranges: The briar dataset. In *WACV*, 2023. 4, 5, 6, 7
- [7] Steve Cruz, Ryan Rabinowitz, Manuel Günther, and Terrance E. Boult. Operational open-set recognition and postmax refinement. In *ECCV*, 2024. 2
- [8] Zhenyu Cui, Jiahuan Zhou, and Yuxin Peng. Dkc: Differentiated knowledge consolidation for cloth-hybrid lifelong person re-identification. In *CVPR*, 2025. 2
- [9] Saeed Ebrahimi, Sahar Rahimi, Ali Dabouei, Srinjoy Das, Jeremy M Dawson, and Nasser M Nasrabadi. Gif: Generative inspiration for face recognition at scale. In *Proceedings of the Computer Vision and Pattern Recognition Conference*, pages 3528–3539, 2025. 2
- [10] Gustav Elfving. The asymptotical distribution of range in samples from a normal population. *Biometrika*, 1947. 2
- [11] Chao Fan, Saihui Hou, Yongzhen Huang, and Shiqi Yu. Exploring deep models for practical gait recognition. *arXiv preprint arXiv:2303.03301*, 2023. 2, 5, 6, 7, 3, 4
- [12] Ronald Aylmer Fisher and Leonard Henry Caleb Tippett. Limiting forms of the frequency distribution of the largest or smallest member of a sample. In *Mathematical proceedings of the Cambridge philosophical society*, 1928. 1
- [13] Chuanxing Geng, Sheng-jun Huang, and Songcan Chen. Recent advances in open set recognition: A survey. *IEEE TPAMI*, 2020. 2
- [14] Boris Gnedenko. Sur la distribution limite du terme maximum d'une serie aleatoire. *Annals of mathematics*, 1943. 1
- [15] Patrick Grother, Mei Ngan, and Kayee Hanaoka. Face recognition vendor test (FRVT) part 2: Identification, 2019. 2
- [16] Xinqian Gu, Hong Chang, Bingpeng Ma, Shutao Bai, Shiguang Shan, and Xilin Chen. Clothes-changing person re-identification with rgb modality only. In *CVPR*, 2022. 2, 5, 7, 3, 4
- [17] Manuel Günther, Steve Cruz, Ethan M Rudd, and Terrance E Boult. Toward open-set face recognition. In *CVPR Workshops*, 2017. 2, 3, 6, 7
- [18] Manuel Günther, Peiyun Hu, Christian Herrmann, Chi-Ho Chan, Min Jiang, Shufan Yang, Akshay Raj Dhamija, Deva Ramanan, Jürgen Beyerer, Josef Kittler, et al. Unconstrained face detection and open-set face recognition challenge. In *IJCB*. IEEE, 2017. 1
- [19] Gavriel Habib, Noa Barzilay, Or Shimshi, Rami Ben-Ari, and Nir Darshan. Cargait: Cross-attention based re-ranking for gait recognition. In *ICCV*, 2025. 2
- [20] Alexander Hermans, Lucas Beyer, and Bastian Leibe. In defense of the triplet loss for person re-identification. *arXiv preprint arXiv:1703.07737*, 2017. 2
- [21] Panjian Huang, Saihui Hou, Junzhou Huang, and Yongzhen Huang. Learning a unified template for gait recognition. In *ICCV*, 2025. 2
- [22] Anil K Jain, Debayan Deb, and Joshua J Engelsma. Biometrics: Trust, but verify. *IEEE Transactions on Biometrics, Behavior, and Identity Science*, 2021. 2
- [23] Anil K. Jain, Arun A. Ross, Karthik Nandakumar, and Thomas Swearingen. *Face Recognition*, pages 119–173. Springer International Publishing, 2025. 1
- [24] Dongyang Jin, Chao Fan, Jingzhe Ma, Jingkai Zhou, Weihua Chen, and Shiqi Yu. On denoising walking videos for gait recognition. In *CVPR*, 2025. 2
- [25] Nathan D Kalka, Brianna Maze, James A Duncan, Kevin O'Connor, Stephen Elliott, Kaleb Hebert, Julia Bryan, and Anil K Jain. IJB-S: IARPA janus surveillance video benchmark. In *BTAS*, 2018. 5, 7, 3, 4
- [26] Wajahat Khalid, Bin Liu, Xulin Li, Muhammad Waqas, and Muhammad Sher Afgan. Bridging the sky and ground: Towards view-invariant feature learning for aerial-ground person re-identification. In *ICCV*, 2025. 2
- [27] Minchul Kim, Anil K Jain, and Xiaoming Liu. Adaface: Quality adaptive margin for face recognition. In *CVPR*, 2022. 2
- [28] Minchul Kim, Feng Liu, Anil K Jain, and Xiaoming Liu. Cluster and aggregate: Face recognition with large probe set. In *NeurIPS*, 2022. 2, 3, 6, 5
- [29] Minchul Kim, Yiyang Su, Feng Liu, Anil Jain, and Xiaoming Liu. Keypoint relative position encoding for face recognition. In *CVPR*, 2024. 4, 7, 3, 5
- [30] Minsoo Kim, Min-Cheol Sagong, Gi Pyo Nam, Junghyun Cho, and Ig-Jae Kim. Vigface: Virtual identity generation for privacy-free face recognition dataset. In *Proceedings of the IEEE/CVF International Conference on Computer Vision*, pages 10043–10053, 2025. 2

[31] Minchul Kim, Dingqiang Ye, Yiyang Su, Feng Liu, and Xiaoming Liu. Sapiensid: Foundation for human recognition. In *CVPR*, 2025. 2

[32] Sunpill Kim, Seunghun Paik, Chanwoo Hwang, Dongsoo Kim, Junbum Shin, and Jae Hong Seo. Idface: Face template protection for efficient and secure identification. In *CVPR*, 2025. 2

[33] Shu Kong and Deva Ramanan. Opengan: Open-set recognition via open data generation. In *ICCV*, 2021. 2

[34] Hari Chandana Kuchibhotla, Sumitra S Malagi, Shivam Chandhok, and Vineeth N Balasubramanian. Unseen classes at a later time? no problem. In *CVPR*, 2022. 2

[35] Longhua Li, Lei Qi, and Xin Geng. One-shot knowledge transfer for scalable person re-identification. In *ICCV*, 2025. 2

[36] Weijia Li, Saihui Hou, Chunjie Zhang, Chunshui Cao, Xu Liu, Yongzhen Huang, and Yao Zhao. An in-depth exploration of person re-identification and gait recognition in cloth-changing conditions. In *CVPR*, 2023. 1, 5, 6, 7, 3, 4

[37] Xin Liang and Yogesh S Rawat. Differ: Disentangling identity features via semantic cues for clothes-changing person re-id. In *CVPR*, 2025. 2

[38] Feng Liu, Ryan Ashbaugh, Nicholas Chimitt, Najmul Hassan, Ali Hassani, Ajay Jaiswal, Minchul Kim, Zhiyuan Mao, Christopher Perry, Zhiyuan Ren, et al. Farsight: A physics-driven whole-body biometric system at large distance and altitude. In *WACV*, 2024. 1, 2, 7

[39] Feng Liu, Minchul Kim, Zhiyuan Ren, and Xiaoming Liu. Distilling CLIP with dual guidance for learning discriminative human body shape representation. In *CVPR*, 2024. 2, 7

[40] Feng Liu, Nicholas Chimitt, Lanqing Guo, Jitesh Jain, Aditya Kane, Minchul Kim, Wes Robbins, Yiyang Su, Dingqiang Ye, Xinguang Zhang, et al. Person recognition at altitude and range: Fusion of face, body shape and gait. *arXiv preprint arXiv:2505.04616*, 2025. 2

[41] Jianbo Ouyang, Hui Wu, Min Wang, Wengang Zhou, and Houqiang Li. Contextual similarity aggregation with self-attention for visual re-ranking. In *NeurIPS*, 2021. 3

[42] Zhiqi Pang, Junjie Wang, Lingling Zhao, and Chunyu Wang. Identity-clothing similarity modeling for unsupervised clothing change person re-identification. In *CVPR*, 2025. 2

[43] Zhengyuan Peng, Jianqiang Xu, Yuge Huang, Jinkun Hao, Shouhong Ding, Zhizhong Zhang, Xin Tan, and Lizhuang Ma. Stylized-face: A million-level stylized face dataset for face recognition. In *ICCV*, 2025. 2

[44] Norman Poh, Samy Bengio, and Jerzy Korczak. A multi-sample multi-source model for biometric authentication. In *Proceedings of the 12th ieee workshop on neural networks for signal processing*. IEEE, 2002. 2

[45] Zhiyuan Ren, Yiyang Su, and Xiaoming Liu. Chatgpt-powered hierarchical comparisons for image classification. *Advances in neural information processing systems*, 36:69706–69718, 2023. 2

[46] Arun Ross, Sudipta Banerjee, Cunjian Chen, Anurag Chowdhury, Vahid Mirjalili, Renu Sharma, Thomas Swearingen, and Shivangi Yadav. Some research problems in biometrics: The future beckons. In *ICB*, 2019. 1

[47] Arun A Ross, Anil K Jain, and Karthik Nandakumar. *Handbook of multibiometrics*. Springer, 2006. 1

[48] M Saquib Sarfraz, Arne Schumann, Andreas Eberle, and Rainer Stiefelhagen. A pose-sensitive embedding for person re-identification with expanded cross neighborhood re-ranking. In *CVPR*, 2018. 3

[49] Chuanfu Shen, Shiqi Yu, Jilong Wang, George Q Huang, and Liang Wang. A comprehensive survey on deep gait recognition: algorithms, datasets and challenges. *arXiv preprint arXiv:2206.13732*, 2022. 1

[50] Chuanfu Shen, Rui Wang, Lixin Duan, and Shiqi Yu. Lidar-gait++: Learning local features and size awareness from lidar point clouds for 3d gait recognition. In *CVPR*, 2025. 2

[51] Xi Shen, Yang Xiao, Shell Xu Hu, Othman Sbai, and Mathieu Aubry. Re-ranking for image retrieval and transductive few-shot classification. In *NeurIPS*, 2021. 3

[52] Yiyang Su, Minchul Kim, Feng Liu, Anil Jain, and Xiaoming Liu. Open-set biometrics: Beyond good closed-set models. In *ECCV*, 2024. 2, 3, 5

[53] Yiyang Su, Yunping Shi, Feng Liu, and Xiaoming Liu. Hamobe: Hierarchical and adaptive mixture of biometric experts for video-based person reid. In *ICCV*, 2025. 2

[54] Yifan Sun, Yifei Ming, Xiaojin Zhu, and Yixuan Li. Out-of-distribution detection with deep nearest neighbors. In *ICML*, 2022. 3

[55] Fuwen Tan, Jiangbo Yuan, and Vicente Ordonez. Instance-level image retrieval using reranking transformers. In *ICCV*, 2021. 3

[56] Sagar Vaze, Kai Han, Andrea Vedaldi, and Andrew Zisserman. Open-set recognition: A good closed-set classifier is all you need. In *ICLR*, 2022. 2

[57] Shining Wang, Yunlong Wang, Ruiqi Wu, Bingliang Jiao, Wenxuan Wang, and Peng Wang. Secap: Self-calibrating and adaptive prompts for cross-view person re-identification in aerial-ground networks. In *CVPR*, 2025. 2

[58] Zitai Wang, Qianqian Xu, Zhiyong Yang, Yuan He, Xiaochun Cao, and Qingming Huang. OpenAUC: Towards AUC-oriented open-set recognition. In *NeurIPS*, 2022. 2

[59] Zengbin Wang, Saihui Hou, Junjie Li, Xu Liu, Chunshui Cao, Yongzhen Huang, Siye Wang, and Man Zhang. Gait-x: Exploring x modality for generalized gait recognition. In *ICCV*, 2025. 2

[60] Kunlun Xu, Fan Zhuo, Jiangmeng Li, Xu Zou, and Jiahuan Zhou. Self-reinforcing prototype evolution with dual-knowledge cooperation for semi-supervised lifelong person re-identification. In *ICCV*, 2025. 2

[61] Jingkang Yang, Pengyun Wang, Dejian Zou, Zitang Zhou, Kunyuan Ding, Wenxuan Peng, Haoqi Wang, Guangyao Chen, Bo Li, Yifan Sun, et al. Openood: Benchmarking generalized out-of-distribution detection. In *NeurIPS*, 2022. 3

[62] Jinxi Yang, He Li, Bo Du, and Mang Ye. Cheb-gr: Rethinking k-nearest neighbor search in re-ranking for person re-identification. In *CVPR*, 2025. 3

[63] Shaopeng Yang, Jilong Wang, Saihui Hou, Xu Liu, Chunshui Cao, Liang Wang, and Yongzhen Huang. Bridging gait recognition and large language models sequence modeling. In *CVPR*, 2025. 2

[64] Dingqiang Ye, Chao Fan, Jingzhe Ma, Xiaoming Liu, and Shiqi Yu. Biggait: Learning gait representation you want by large vision models. In *CVPR*, 2024. 2, 5, 6, 7, 3, 4

[65] Dingqiang Ye, Chao Fan, Zhanbo Huang, Chengwen Luo, Jianqiang Li, Shiqi Yu, and Xiaoming Liu. Biggergait: Un-locking gait recognition with layer-wise representations from large vision models. In *NeurIPS*, 2025. 2

[66] Jinghan You, Shanglin Li, Yuanrui Sun, Jiangchuan Wei, Mingyu Guo, Chao Feng, and Jiao Ran. Lvface: Progressive cluster optimization for large vision models in face recognition. In *ICCV*, 2025. 2

[67] Chao Yuan, Guiwei Zhang, Changxiao Ma, Tianyi Zhang, and Guanglin Niu. From poses to identity: Training-free person re-identification via feature centralization. In *CVPR*, 2025. 2

[68] Asmat Zahra, Nazia Perwaiz, Muhammad Shahzad, and Muhammad Moazam Fraz. Person re-identification: A retrospective on domain specific open challenges and future trends. *Pattern Recognition*, 2023. 1

[69] Xiao-Wen Zhang, Delong Zhang, Yi-Xing Peng, Zhi Ouyang, Jingke Meng, and Wei-Shi Zheng. Viperson: Flexibly generating virtual identity for person re-identification. In *ICCV*, 2025. 2

[70] Yuqi Zhang, Qi Qian, Hongsong Wang, Chong Liu, Weihua Chen, and Fan Wang. Graph convolution based efficient re-ranking for visual retrieval. *IEEE Transactions on Multimedia*, 2023. 3

[71] Jinkai Zheng, Xincheng Liu, Wu Liu, Lingxiao He, Chenggang Yan, and Tao Mei. Gait recognition in the wild with dense 3d representations and a benchmark. In *CVPR*, 2022. 5, 6, 7, 3, 4

[72] Zhun Zhong, Liang Zheng, Donglin Cao, and Shaozi Li. Re-ranking person re-identification with k-reciprocal encoding. In *CVPR*, 2017. 3, 7, 4

[73] Jie Zhu, Yiyang Su, Minchul Kim, Anil Jain, and Xiaoming Liu. A quality-guided mixture of score-fusion experts framework for human recognition. In *ICCV*, 2025. 2

LocalScore: Local Density-Aware Similarity Scoring for Biometrics

Supplementary Material

A. Effect on Rank-1 Accuracy

The effect of Alg. 1 on rank-1 accuracy can be summarized in the following theorem:

Theorem 2. *Let s_1, s_2, \dots, s_n denote a set of similarity scores produced by a closed-set recognition algorithm, where s_i represents the similarity score between a probe and the i -th gallery subject. If Alg. 1 adds a non-negative value d to the highest score, the closed-set accuracy at any rank does not change.*

Proof. To show this, we can assume without loss of generality that the scores are in non-decreasing order, *i.e.*, $s_1 \leq s_2 \leq \dots \leq s_n$. By Alg. 1, the highest score s_n is modified to $s_n + d$, where $d \geq 0$. This results in the following inequality:

$$s_1 \leq s_2 \leq \dots \leq s_n \leq s_n + d. \quad (10)$$

This adjustment preserves the relative ranking of the scores.

The closed-set accuracy at rank r is determined by the number of correct matches among the top r scores. Suppose the correct match corresponds to the score s_j . If s_j is initially ranked within the top r , we have $j \geq n + 1 - r$. As the adjustment preserves relative ranking, s_j remains correctly ranked within the top r . Conversely, if s_j is not among the top r scores initially, then $j < n + 1 - r$. The increase in s_n does not affect the ranks of other scores below s_n , ensuring s_j continues to be unranked within the top r .

In both cases, we conclude that Alg. 1 does not change the closed-set accuracy at any rank. Q.E.D.

B. Proof of Thm. 1

In this section, we provide a proof of Thm. 1. Before the proof, we reproduce the theorem below for your reference.

Suppose the per-subject genuine scores are normally distributed as $\mathcal{N}(\mu_1, \sigma_1)$. The per-subject imposter scores are distributed as $\mathcal{N}(\mu_2, \sigma_2)$. The KNN scores for mated probes are distributed as $\mathcal{N}(\mu_3, \sigma_3)$, and the KNN scores for non-mated probes are distributed as $\mathcal{N}(\mu_4, \sigma_4)$. Also, let N_1 be the number of mated probes, N_2 be the number of non-mated probes, M is the number of gallery subjects, N_3 be the total number of imposter scores, and r_1 and r_2 be the tolerable number of maximum-per-probe non-mated scores (*e.g.*, $0.1\% \times N_2$) and non-match scores (*e.g.*, $0.1\% \times N_3$).

Theorem 1. *Alg. 1 improves the expected open-set*

FNIR@FPIR at the expected threshold if

$$\frac{\mu_2 + \mu_4 + \delta \sqrt{\sigma_2^2 + \sigma_4^2} - (\mu_1 + \mu_3)}{\sqrt{\sigma_1^2 + \sigma_3^2}} < \frac{(\mu_2 + \delta \sigma_2) - \mu_1}{\sigma_1}, \quad (5)$$

where $\delta = -\ln(-\ln(1 - r_1/N_2))$ and improves verification TAR@FAR at the expected threshold if

$$\frac{\mu_2 + \mu_4 + \Phi^{-1}\left(\frac{N_3 - r_2 - \alpha}{N_3 - 2\alpha + 1}\right) \sqrt{\sigma_2^2 + \sigma_4^2} - (\mu_1 + \mu_3)}{\sqrt{\sigma_1^2 + \sigma_3^2}} \\ < \frac{\mu_2 + \Phi^{-1}\left(\frac{N_3 - r_2 - \alpha}{N_3 - 2\alpha + 1}\right) \sigma_2 - \mu_1}{\sigma_1}, \quad (6)$$

where $\Phi^{-1}(\cdot)$ is the inverse of the cumulative distribution function of normal distribution, and $\alpha = \pi/8$ is a constant.

Proof. We prove the two parts of the theorem, namely Eq. (7) and Eq. (8) separately and we start with Eq. (7).

To prove Eq. (7), we begin by considering the FNIR threshold without KNN scores. By the Fisher-Tippett-Gnedenko theorem [12, 14], since the non-match scores follow a Gaussian distribution, the maximum non-mated scores converge to a Gumbel distribution.

Given the mean of non-match scores without KNN scores μ_2 and its standard deviation is σ_2 , the corresponding threshold is determined by the quantile of the Gumbel distribution. Specifically, the threshold for FPIR equal to $\frac{r_1}{N_2}$ is given by:

$$\mu_2 + \left(-\ln -\ln \left(1 - \frac{r_1}{N_2} \right) \right) = \mu_2 + \delta \sigma_2, \quad (11)$$

if we let $\delta = -\ln \left(-\ln \left(\frac{r_1}{N_2} \right) \right)$, which is the critical value corresponding to the desired FPIR. This threshold is derived from the inverse cumulative distribution function (CDF) of the Gumbel distribution.

Next, to compute the FNIR at this threshold, we use the fact that the match scores follow a Gaussian distribution with mean μ_1 and standard deviation σ_1 . The FNIR is then given by the complementary cumulative distribution function of the match scores at the threshold:

$$\text{FNIR} = 1 - \Phi \left(\frac{(\mu_2 + \delta \sigma_2) - \mu_1}{\sigma_1} \right), \quad (12)$$

where Φ is the CDF of the standard normal distribution. This is the expected FNIR at the threshold based on the original match scores.

Now, we introduce KNN scores. When KNN scores are used, the non-match scores become a sum of two Gaussian distributions: one with mean μ_2 and variance σ_2^2 , and the other with mean μ_4 and variance σ_4^2 . The resulting distribution is Gaussian with mean $\mu_2 + \mu_4$ and standard deviation $\sqrt{\sigma_2^2 + \sigma_4^2}$.

Thus, the FPIR threshold with KNN scores is given by

$$\mu_2 + \mu_4 + \delta \sqrt{\sigma_2^2 + \sigma_4^2}. \quad (13)$$

Similarly, the FNIR with KNN scores at the expected threshold is

$$\text{FNIR}_{\text{KNN}} = 1 - \Phi \left(\frac{\mu_2 + \mu_4 + \delta \sqrt{\sigma_2^2 + \sigma_4^2} - (\mu_1 + \mu_3)}{\sqrt{\sigma_1^2 + \sigma_3^2}} \right), \quad (14)$$

where $\mu_1 + \mu_3$ is the mean of the match scores with KNN, and $\sqrt{\sigma_1^2 + \sigma_3^2}$ is the standard deviation. Here it is assumed for simplicity that the KNN scores are added to all match scores, which is a reasonable assumption for real-world biometric systems.

To prove the first part of the theorem, we show that Alg. 1 improves the FNIR. This is equivalent to showing that the FNIR with KNN scores is smaller than the FNIR without KNN scores. To do so, we compare the arguments inside the CDFs of the two FNIR expressions. Specifically, we require:

$$\frac{\mu_2 + \mu_4 + \delta \sqrt{\sigma_2^2 + \sigma_4^2} - (\mu_1 + \mu_3)}{\sqrt{\sigma_1^2 + \sigma_3^2}} < \frac{(\mu_2 + \delta \sigma_2) - \mu_1}{\sigma_1}. \quad (15)$$

This inequality guarantees that the FNIR with KNN scores is smaller (improved) compared to the FNIR without KNN scores. Since $\Phi(\cdot)$ is a monotonically increasing function, the inequality implies that the FNIR with KNN scores is indeed lower.

Next, we turn to the second part of the theorem: improving the verification TAR@FAR at the expected threshold. We begin by deriving the FAR threshold for the non-match scores, which follow a Gaussian distribution with mean μ_2 and standard deviation σ_2 . By [10], the FAR threshold for a given false acceptance rate $\frac{r_2}{N_3}$ is given by:

$$\mu_2 + \Phi^{-1} \left(\frac{N_3 - r_2 - \alpha}{N_3 - 2\alpha + 1} \right) \sigma_2. \quad (16)$$

where $\alpha = \frac{\pi}{8}$ is a constant and Φ^{-1} is the inverse of the standard normal CDF.

For verification TAR, we assume that Alg. 1 adds the KNN scores to all non-match scores above this threshold. Thus, the new expected verification threshold becomes:

$$\mu_2 + \mu_4 + \Phi^{-1} \left(\frac{N_3 - r_2 - \alpha}{N_3 - 2\alpha + 1} \right) \sqrt{\sigma_2^2 + \sigma_4^2}. \quad (17)$$

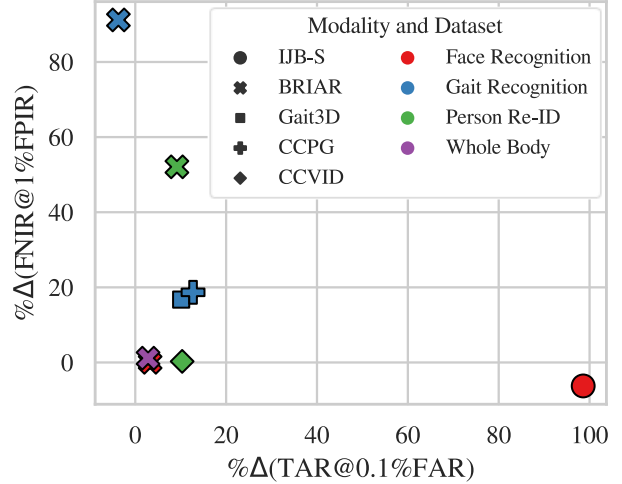


Figure 7. The relative performance improvement ($\% \Delta$) of LocalScore on different modalities and datasets is calculated as $(\text{ours} - \text{baseline}) / \text{baseline}$, where “ours” represents TAR@0.1%FAR or FNIR@1%FPIR with LocalScore, and “baseline” refers to the corresponding values without LocalScore. A value of $(0, 0)$ indicates no improvement over the baseline in either metric. These results, derived from Tab. 2, highlight the performance gains achieved by our approach.

Finally, we compare the z-scores of the verification thresholds with and without KNN scores. The z-score for the match score distribution (without KNN) is:

$$\frac{\mu_2 + \mu_4 + \Phi^{-1} \left(\frac{N_3 - r_2 - \alpha}{N_3 - 2\alpha + 1} \right) \sqrt{\sigma_2^2 + \sigma_4^2} - (\mu_1 + \mu_3)}{\sqrt{\sigma_1^2 + \sigma_3^2}}. \quad (18)$$

For the case with KNN scores, the z-score is:

$$\frac{\mu_2 + \mu_4 + \Phi^{-1} \left(\frac{N_3 - r_2 - \alpha}{N_3 - 2\alpha + 1} \right) \sigma_2 - \mu_1}{\sigma_1}, \quad (19)$$

By comparing the z-scores of the two distributions, we conclude that Alg. 1 improves the verification TAR@FAR at the expected threshold if Eq. (8) holds. Q.E.D.

C. Additional Experiments

Relative Performance Improvement Fig. 7 presents the results of Tab. 2 visually: the percentage of performance improvement compared to baselines on different modalities and datasets. LocalScore achieves significant performance improvements across all datasets, enhancing either verification TAR@0.1%FAR or FNIR@1%FPIR. Notably, it improves verification by approximately 100% on the challenging IJB-S face recognition dataset and boosts gait recognition performance by about 90% on BRIAR. Overall, LocalScore

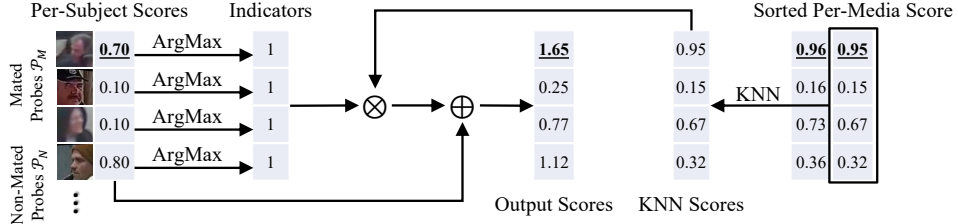


Figure 8. Illustration of single-subject evaluation using LocalScore. Compared to Fig. 2, when only one gallery subject is available, the indicators are always 1 since each probe has only one per-subject score. Therefore, the k -th largest score of the same subject is added to the per-subject scores.

Model	Dataset	Mod.	C_i	% Gal.	Run-time	FNIR@FPIR ↓		TAR@FAR ↑	
						0.1%	1%	0.1%	1%
KPRPE [29]	IJB-S [†] [25]	Face	N/A 5 20 ∞	< 1 6.3 23.4 100	148 285 595 94.49	94.11	88.64	10.69	25.47
						93.77	88.81	21.88	45.27
						94.50	88.57	22.14	45.62
						94.49	89.12	21.76	45.46
SwinGait [11]	Gait3D [†] [71]	Gait	N/A 5 20 ∞	< 1 53.7 92.3 100	124 246 319 338	81.84	66.09	57.81	78.95
						83.50	69.10	63.65	78.95
						81.01	65.43	63.65	79.08
						78.80	62.98	63.65	79.08
BigGait [64]	CCPG [36]	Gait	N/A 5 20 ∞	< 1 14.2 56.8 100	29 60 175 301	46.95	34.53	82.46	95.64
						41.04	29.52	92.25	97.00
						39.23	27.34	92.89	97.00
						37.04	25.34	92.95	97.01
CAL [16]	CCVID [†] [16]	ReID	N/A 5 20 ∞	< 1 60.8 100 100	15 31 41 41	39.98	34.38	68.19	81.81
						38.39	33.72	75.69	85.34
						38.98	34.19	75.23	85.34
						38.98	34.19	75.23	85.34

Table 5. Open-set FNIR@FPIR and verification TAR@FAR under different C_i . % Gal.: the ratio of the size of the clustered gallery to that of the full gallery. Runtime is reported in milliseconds (ms). [†]FNIR@FPIR reported at 1% and 5% thresholds.

demonstrates greater performance gains in gait recognition and person reID, where open-set biometrics pose greater challenges, while also delivering improvements in face recognition. These results highlight the effectiveness and generalizability of our approach across diverse biometric tasks.

C.1. 1:1 Evaluation.

The key distinction between the 1:1 and standard evaluation settings lies in the assumed availability of gallery data. Standard evaluation follows the conventional biometric protocol in which all enrolled subjects’ galleries are accessible for both verification and retrieval. This reflects typical operational scenarios, where a complete gallery is pre-enrolled prior to deployment; even in verification, galleries of non-claimed subjects are available, though they are not explicitly used by most systems. In extremely constrained environments, however, access to galleries of irrelevant subjects may be restricted. To assess LocalScore under such condi-

tions, we additionally evaluate performance in the 1:1 setting, where only the gallery samples of the claimed identity are provided.

As illustrated in Fig. 8, this scenario yields a single column of per-subject scores that reflect the sole accessible gallery and fewer per-media scores compared to Fig. 2, since non-claimed identities’ media are excluded. Consequently, all indicators evaluate to 1, as each is computed via an argmax over a single value, and the k -NN scores are added to the per-subject scores. Despite these constraints, Tab. 2 shows that LocalScore continues to improve the performance of multiple biometric models across modalities in both open-set retrieval and verification.

C.2. Gallery Clustering

Tab. 5 shows that increasing C_i —which corresponds to using a larger portion of the clustered gallery—generally improves both open-set and verification performance across all models

Task	Model	Dataset	Mod.	Method	FNIR@FPIR ↓		TAR@FAR ↑	
					0.1%	1%	0.1%	1%
Face	KPRPE [29]	IJB-S [†] [25]	Face	Max	95.39	89.80	8.73	22.40
				Min	99.83	99.11	1.40	7.45
				Mean	96.14	90.92	9.55	25.06
				R-R	95.32	92.45	8.69	23.98
				Ours	94.49	89.12	21.76	45.47
Gait	SwinGait [11]	Gait3D [71]	Gait	Max	81.92	60.40	70.66	91.11
				Min	88.02	73.24	50.99	78.34
				Mean	83.72	60.81	74.00	93.73
				R-R	82.84	67.61	56.96	77.98
				Ours	78.80	62.98	63.65	79.08
Gait	BigGait [64]	CCPG [36]	Gait	Max	42.87	28.92	86.94	97.11
				Min	83.23	70.97	48.65	77.88
				Mean	51.08	38.12	79.22	95.20
				R-R	47.84	36.56	81.12	95.14
				Ours	37.04	25.34	92.95	97.01
ReID	CAL [16]	CCVID [†] [16]	ReID	Max	40.55	32.89	69.65	82.83
				Min	54.49	45.86	60.97	80.36
				Mean	38.74	34.38	69.16	82.87
				R-R	40.52	34.12	68.88	83.60
				Ours	38.98	34.19	75.23	85.34

Table 6. Open-set FNIR@FPIR and verification TAR@FAR of multi-sample methods. [†]FNIR@FPIR reported at 1% and 5% thresholds. [R-R: Re-ranking [72]]

and modalities, while introducing only moderate runtime overhead. In the baseline setting ($C_i = \text{N/A}$), where less than 1% of the gallery is used, performance is consistently lower. As C_i increases, FNIR decreases and TAR increases, with most models achieving their best or near-best results when leveraging the full gallery ($C_i = \infty$). This trend is especially pronounced for gait and ReID models: BigGait on CCPG, for example, sees FNIR@0.1% drop from 46.95% to 37.04% and TAR@0.1% rise from 82.46% to 92.95%. Similar improvements appear for SwinGait on Gait3D and CAL on CCVID. For face recognition on IJB-S, the gains plateau earlier, with $C_i = 20$ already matching or surpassing the full-gallery setting. Overall, the results indicate that incorporating a larger clustered gallery consistently enhances recognition performance across diverse biometric modalities, while the additional computation remains manageable for real-world deployment.

C.3. Comparison to multi-sample methods

Tab. 6 compares LocalScore with conventional multi-sample aggregation strategies across face, gait, and ReID tasks. Overall, the results show that pooling-based methods such as max, mean, and min exhibit inconsistent behavior: max often provides competitive FNIR but relatively weaker TAR, while mean generally improves verification performance but struggles in open-set conditions. Min performs worst across all settings, confirming its sensitivity to outliers. Re-ranking

(R-R) offers moderate improvements but remains limited by its reliance on reciprocal neighbors and multiple probes. In contrast, LocalScore delivers strong and consistent gains, particularly in challenging open-set scenarios. For instance, on CCPG gait, LocalScore reduces FNIR@0.1% FPIR to 37.04%, markedly outperforming max (42.87%) and mean (51.08%), while also achieving the highest TAR@0.1% FAR (92.95%). Similar improvements appear in face and ReID settings, where LocalScore achieves the best or near-best performance across all metrics. These results highlight the advantage of incorporating local gallery structure into the scoring function, enabling more reliable recognition than traditional aggregation or re-ranking methods.

C.4. Statistical Significant Tests

We perform two-sample t-tests to evaluate whether the performance gains achieved with LocalScore are statistically significant across random mated-vs-non-mated splits, as shown in Tab. 7. The results indicate that all improvements in gait recognition are highly significant, with most p -values smaller than 0.0001. Although the improvements on the CAL model for the CCVID dataset are less significant, LocalScore still achieves notable verification gains over CAL, which demonstrates its effectiveness. On other datasets, the large probe set sizes reduce random fluctuations.

Model	Dataset	Gallery	FNIR@FPIR		TAR@FAR	
			1%	5%	0.1%	1%
SwinGait	Gait3D	Avg+Euc	0.0001	0.0001	0.0001	0.0001
		EVM	0.6441	0.3295	0.0001	0.3120
BigGait	CCPG	Avg+Euc	0.0001	0.0001	0.0001	0.0001
		EVM	0.0167	0.0014	0.0001	0.0001
CAL	CCVID	Avg+Cos	0.0001	0.4077	0.0001	0.0001
		EVM	1.0000	0.0012	0.0001	0.6741

Table 7. FNIR@FPIR, TAR@FAR, and their statistical significance tests on real-world biometric datasets.

Modality	Model	Dataset	Gallery	Post-proc.	FNIR@FPIR ↓		TAR@FAR ↑		R@1 ↑
					0.1%	1%	0.1%	1%	
Face	KPRPE [29]	BRIAR [‡] [6]	CAFace [28]	N/A	65.55	54.93	59.93	72.52	84.34
				+const.	65.55	55.00	61.64	72.39	84.34
				×2	65.55	55.00	61.64	72.52	84.34
				1,2-NN	64.99	54.85	61.82	72.52	84.34
				1,2,3-NN	65.12	54.91	62.01	72.52	84.34
				Ours	64.81	54.91	61.89	72.52	84.34
Gait	SwinGait [11]	Gait3D [†] [71]	Avg + Euc	N/A	81.84±1.76	66.09±0.69	57.81	78.95	72.2
				+const.	81.85±1.75	66.46±0.64	63.65	79.08	72.2
				×2	81.85±1.75	66.46±0.64	63.65	79.08	72.2
				1,2-NN	80.19±1.85	64.69±0.61	63.65	79.08	72.2
				1,2,3-NN	81.78±1.65	66.34±0.61	63.65	79.08	72.2
				Ours	78.80±1.99	62.98±0.78	63.65	79.08	72.2

Table 8. Open-set FNIR@FPIR, verification TAR@FAR, and closed-set Rank-1 accuracy on real-world biometric datasets. 95% confidence intervals are reported for FNIR@FPIR. [†]FNIR@1%FPIR and FNIR@5%FPIR are reported. [‡]Rank-20 accuracy is reported according to the official evaluation protocol [Keys: R@ 1=rank-1 accuracy]

C.5. Effect of KNN scores

We conduct additional experiments to analyze the effects of KNN scores on the original score matrices using several variations. First, we add a constant 1 to the highest score for each probe, which does not introduce additional discriminability between mated and non-mated probes (“+const.”). Second, we replace the highest score for each probe with twice its value, increasing its magnitude while maintaining limited discriminability between mated and non-mated probes but without leveraging KNN scores (“×2”). Third, we use the average of the 2 nearest neighbors (1,2-KNN) or the 3 nearest neighbors (1,2,3-KNN).

As shown in Tab. 8, while all these approaches improve verification performance, none surpasses our proposed method. For open-set FNIR@FPIR, none of these variations outperforms LocalScore on Gait3D. Furthermore, on face recognition, the “+const.” and “×2” approaches fail to improve open-set performance, highlighting the necessity of incorporating KNN information for better open-set results. Including more nearest neighbors yields comparable results when all neighbors provide reasonable performance, as in

face recognition. However, this strategy performs worse for gait recognition, where additional nearest neighbors contribute lower-quality information. In general, we conclude that KNN scores are both crucial and effective for improving verification and open-set performance.

D. Additional Analyses

D.1. Additional Analyses on Thm. 1

Building on the analysis in Fig. 5, we examine how Eq. (8) provides insights into real-world verification performance, focusing on the impact of μ_3 . Using the same experimental setup as Fig. 5a, we analyze how variations in μ_3 influence performance, with μ_3^{**} denoting the value where the LHS and RHS of Eq. (8) are equal. The results confirm that the theoretically predicted μ_3^{**} closely aligns with the real-world value where applying LocalScore has no effect on performance. When $\mu_3 < \mu_3^{**}$, LocalScore decreases verification performance, whereas for $\mu_3 > \mu_3^{**}$, it improves performance.

Fig. 9b shows how the difference between the RHS and LHS of Eq. (8) influences TAR@0.1%FAR, with larger dif-

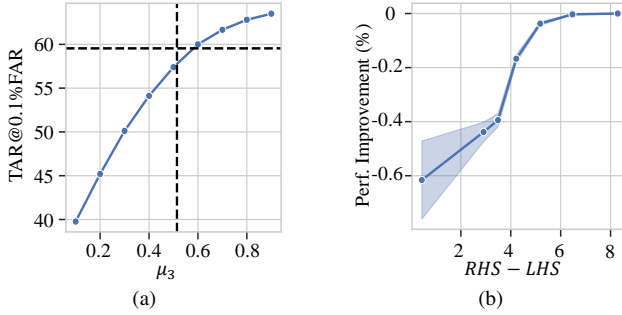


Figure 9. (a) The effect of μ_3 on TAR@0.1%FAR. The vertical dashed line indicates the theoretically predicted μ_3^{**} , and the horizontal line indicates the performance without LocalScore. (b) The impact of the difference between the RHS and LHS of Eq. (8) on the improvement of TAR@0.1%FAR by using LocalScore. The shaded area is the 99% confidence interval.

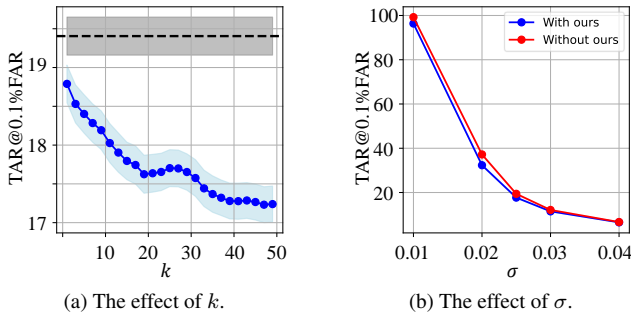


Figure 10. The effect of k and σ on TAR@0.1%FAR. In (a), the horizontal line denotes performance without LocalScore. The shaded area is the 99% confidence interval.

ferences generally leading to greater improvements. However, verification performance slightly declines with KNN, likely due to a larger offset between actual and theoretical μ_3 values in Fig. 9a, where no improvement is predicted. This may result from the stronger impact of the normality assumptions in Eq. (8) on verification compared to open-set biometrics, as also observed in Fig. 10, where KNN often worsens performance. Despite this, LocalScore consistently enhances verification on real-world biometric datasets, as demonstrated in Fig. 7, with significant improvements except for gait recognition on BRIAR. This indicates that while Eq. (7) offers practical guidance for real-world scenarios, Eq. (8) is less effective in predicting performance improvements with LocalScore.

D.2. Additional Ablation Study

Fig. 10 illustrates the effect of LocalScore on verification performance using synthetic datasets. In Fig. 10a, TAR@0.1%FAR shows a gradual decrease as k increases, but the decrease is minimal—at worst about 2%—compared to the significant improvement of FNIR@1%FPIR in Fig. 4(a), which reaches approximately 15%. This demonstrates

that LocalScore substantially enhances open-set performance with only slightly reducing verification performance on randomly generated features.

Fig. 10b examines the impact of σ , which governs intra-class variation, on verification performance. As σ increases, intra-class variation grows, and the performance gap between using and not using LocalScore narrows. Importantly, our approach achieves comparable verification performance to the baseline, even with higher σ . This demonstrates that LocalScore enhances open-set performance without compromising verification, providing a balanced and comprehensive evaluation of biometric systems.

E. Limitations

LocalScore assumes that gallery media are well-distributed and provide a reasonable approximation of the actual gallery feature distribution. While this assumption may not always hold in real-world scenarios, we introduce a theoretical framework (Thm. 1) that predicts whether LocalScore will improve verification and open-set biometric performance. We validate this framework on real-world datasets as well as on randomly generated features and scores. In practice, a small test set can be used to assess the potential performance gains of LocalScore before deployment.

Our scoring algorithm requires additional storage for per-media features, but this demand is manageable due to several factors. Biometric features are typically compact, and high-capacity storage is increasingly affordable. Additionally, clustering the gallery samples can reduce storage load without significantly sacrificing performance, and cloud-based storage is scalable and cost-effective in handling data without local limitations.

F. Potential Societal Impacts

While our work advances biometric technologies with potential benefits in security and forensics, it also raises concerns about privacy and individual freedoms. Sensitive biometric data, such as facial features, could be misused for unauthorized surveillance or profiling, which severely erodes public trust and infringes on rights. We prioritize using data collected with informed consent and avoid collecting any biometric data directly. We urge the community to adopt transparent and responsible practices to ensure that biometrics serve society positively while minimizing potential harm.